# Bone Fragment Segmentation From 3D CT Imagery

Waseem G. Shadid, Andrew Willis

*Electrical and Computer Engineering Department, The University of North Carolina at Charlotte, 9201 University City Blvd., Charlotte, NC USA*

**Abstract**

This paper presents a novel method to segment bone fragments imaged using 3D Computed Tomography (CT). Existing image segmentation solutions often lack accuracy when segmenting internal trabecular and cancellous bone tissues from adjacent soft tissues having similar appearance and often merge regions associated with distinct fragments. These issues create problems in downstream visualization and pre-operative planning applications and impedes the development of advanced image-based analysis methods such as virtual fracture reconstruction. The proposed segmentation algorithm uses a probability-based variation of the watershed transform, referred to as the Probabilistic Watershed Transform (PWT). The PWT uses a set of probability distributions, one for each bone fragment, that model the likelihood that a given pixel is a measurement from one of the bone fragments. The likelihood distributions proposed improve upon known shortcomings in competing segmentation methods for bone fragments within CT images. A quantitative evaluation of the bone segmentation results are provided that compare our segmentation results with several leading competing methods as well as human-generated segmentations.

*Keywords:* Segmentation, 3D, Computed Tomography (CT), Bone, Fragment, Watershed transform.

*Email addresses:* wshadid78@gmail.com (Waseem G. Shadid), arwillis@uncc.edu (Andrew Willis)

*URL:* visionlab.uncc.edu (Andrew Willis)

## 1. Introduction

The images generated by contemporary 3D Computerized Tomography (CT) scans are essential tools for providing diagnostic medical information. The segmentation task seeks to divide these images into semantically-meaningful regions. Segmenting images manually is a very time consuming, tedious, and subjective process because of the huge amount of data and variations in expert's opinions Fornaro et al. (2010). Computational segmentation algorithms seek to address these issues by performing this task automatically. Bone fragment segmentation is achieved by either identifying all pixels that belong to the bone fragment or locating the pixels that form the fragment surface boundary. Bone fragment segmentation is an essential process in the medical field as it allows users to visualize and analyze bone fracture structures which may be difficult to observe from images alone. This facilitates improvements to fracture diagnosis and treatment planning.

Bone fragment segmentation is a challenging problem. Bone fragmentation creates distinct bone fragments whose boundary typically consists of both cortical and cancellous tissues. This context requires a new model for accurate bone fragment segmentation. Further, the scaffold-like structure of cancellous tissue exhibits significantly lower CT intensities than the cortical tissues. In regions where the scaffold includes large voids, e.g., the metaphysis/epiphysis, these intensities often overlap with those of neighboring anatomical structures such as muscle, tendons and fat.

While many algorithms have been developed for bone segmentation as in Arabi and Zaidi (2017); Chu et al. (2015); Perez-Carrasco et al. (2015); Wu et al. (2014); Paulano et al. (2014); Schmid et al. (2011); Swierczynski et al. (2017); Brahim et al. (2017), very few of them include models appropriate for the challenges associated with segmenting bone fragments. Most approaches have the goal of segmenting intact bones from CT imagery and not bone fragments which pose unique challenges.

The proposed work is an example of an automatic algorithm to segment bone fragments within CT images of traumatic bone fractures, i.e., fractures which separate a bone into multiple fragments (3 or more). This paper addresses two of the key challenges associated with bone fragment segmentation (1) segmenting internal trabecular and cancellous bone tissues from adjacent soft tissues having similar appearance and (2) separating bone fragments that touch. The proposed approach formulates new probabilstic models to improve state-of-the-art for segmenting bone fragments from fracture CT

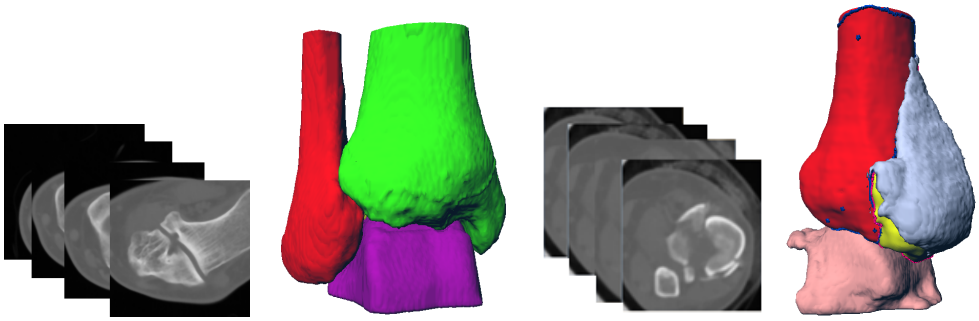

(a) (b) (c) (d)

Figure 1: (a) shows slices from a 3D CT image of an intact ankle joint. (b) shows the segmented tibia, fibula, and talus bone surfaces. (c) shows slices from a 3D CT image of a fractured ankle. (d) shows the segmented bone fragments surfaces. The segmentation from the 3D CT image was performed using the proposed segmentation algorithm.

data. Segmentation proceeds by incrementally classifying pixels from image regions of high-likelihood to regions of lower likelihood. The segmentation algorithm applies a probability-based version of the watershed algorithm to expand regions along constant contours of probability/likelihood. This version of the watershed algorithm is referred to as the Probabilistic Watershed Transform (PWT). The majority of pixels are classified using a pixel-to-fragment class-conditional likelihood function which considers unclassified pixels spatial proximity and intensity similarity to candidate fragments. A second "isthmus" class-conditional likelihood function serves to segment a small subset of the image data where island-like (hence "isthmus") portions of trabecular bone tissue is found far from candidate bone fragments. A third probability function serves to switch between the pixel-to-fragment and "isthmus" classification models. Figure (1) shows two 3D segmentations of an ankle joint and a fractured ankle joint using the proposed algorithm. This work extends preliminary work from Shadid and Willis (2013) which proposed the approach for 2D image data. This paper describes new likelihood models and presents new results for 3D image data.

This paper is organized as follows: Section 2 reviews state-of-the-art in computer based bone fracture analysis systems and medical image segmentation algorithms. Section 3 describes the bone fragment segmentation algorithm used to segment fragments within a 3D CT image of a fractured

limb. Section 4 provides segmentation results for clinical fracture cases and quantitatively compares these results with several competing methods and with human-generated segmentations. Section 5 concludes the paper with a summary of the work and its impact on the current state of the research in this field.

## 2. Related Work

A need for accurate bone segmentation from CT imagery has made this general topic a long-standing research interest for several decades. As mentioned earlier, most approaches have the goal of segmenting intact bones from CT imagery and not bone fragments which pose unique challenges. Li et.al. in Li et al. (2015) proposed a fully automated intact cortical bone segmentation algorithm for in vivo MD-CT imaging of human distal tibia. The algorithm uses digital topologic and geometric techniques to perform bone filling, alignment, region computation, and cortical bone segmentation. Valentinitsch et. al. in Valentinitsch et al. (2012) proposed an automated threshold independent technique to segment intact cortical and trabecular bone in High Resolution peripheral Quantitative CT (HR-pQCT) images. The algorithm uses local texture features to train a random forest classifier to distinguish between cortex pixels and trabecular ones. Burghardt et. al. in Burghardt et al. (2007) introduced an an adaptive local thresholding approach using a hysteresis algorithm on a gradient map. This approach is applied to segment intact trabecular bone in HR-pQCT images. Chen et. al. in Chen et al. (2017) developed a diffusion algorithm that depends on computing the bone morrow contrast and the spatial variation in the background marrow intensity. The algorithm was applied to segment intact trabecular bone in vivo CT images. These algorithms have been developed to segment intact bones within high quality CT images.

These approaches have significantly advanced the state-of-the-art for accurately labeling bone tissue in CT. Yet, these methods often produce inaccurate results when applied to segment bone fragments generated by a long bone fracture. This can be explained by the fact that these algorithms make the "envelope assumption". This assumption is motivated by the fact that intact bones consist of a dense outer shell of cortical bone tissue which acts as an envelope for the less-dense cancellous bone tissue (also known as trabecular or spongy bone tissue) inside, see figure (2). Segmentation methods for intact, i.e., non-fractured bones using the envelope assumption target de-

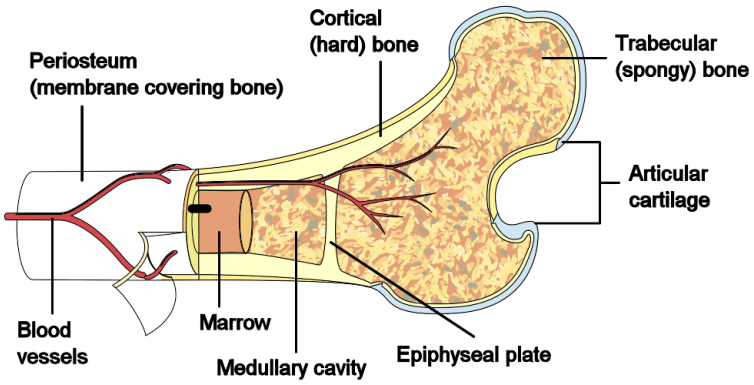


Figure 2: Shows the typical anatomy of intact bone tissue where dense cortical tissues surround less-dense cancellous tissue. Image created by Pbroks13 02:26, 27 November 2008 (UTC)

tection of the high-intensity cortical tissues that form the outer envelope of the bone tissue. The less-distinctive cancellous bone tissue regions internal to the bone at the bone ends can be classified, if necessary, as it is enclosed inside this envelope. The envelop assumption greatly simplifies bone segmentation as it allows the surface of bones to be detected and it also facilitates separation of adjacent bones at joint locations. When the outer envelope of cortical tissue is disrupted, as is the case in a bone fracture, the envelope assumption is no longer valid which creates problems for these approaches which manifest as inaccuracies in the bone fragment shapes and merging of adjacent bone fragments into a single bone tissue region. This problem likely to appear at close proximity areas where small parts of different bone fragments with small depth appear touching each other in a CT image, see figure (3).

Our approach adopts a model for bone tissue applicable for segmentation of both intact and fractured bone tissues albeit the most significant contribution of this approach is for segmenting fractured bone tissues. Specifically, we extend a technique originally proposed by Grau et. al. in Grau et al. (2004) which proposes integrating probability theory with the classical watershed transform segmentation algorithm. In their paper, the authors demonstrate that difficult medical image segmentation problems may be solved using this approach while avoiding many of the pitfalls typically associated with watershed transform with specific examples that include segmentation of a knee

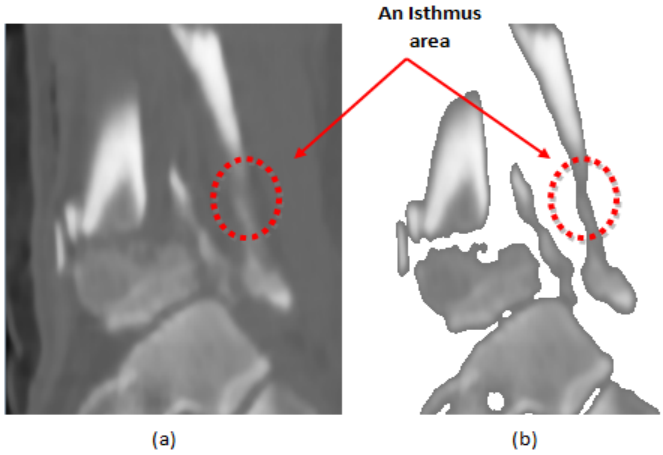


Figure 3: An example of an "isthmus" of bone area. (a) A CT image of a fractured bone. (b) An image of the estimated bone region. Circled area shows a location for an "isthmus" of bone area where two bone fragments are touching. An "isthmus" area has a small width compared to other bone region areas.

joint MRI into cartilage, bone, and other tissues and segmentation of a brain MRI into cerebral spinal fluid, white matter, and grey matter.

In Grau et al. (2004), a very conservative classifier is used to assign labels to those pixels in the image whose object class can be estimated with very high confidence. These pixels are used as region seeds for each object class which are expanded, using the watershed transform algorithm, along constant (discrete) contours of probability using the posterior probability of the object class. The posterior probability is computed via Bayes rule. This rule takes the posterior probability of the class, $k$, given the data, $\mathcal{D}$, as the product of a prior distribution on the class $k$ denoted $P(k)$ and a conditional likelihood function $P(\mathcal{D}|k)$ normalized by the probability of observations, $P(\mathcal{D})$. $P(\mathcal{D})$ is typically written as a marginalized joint distribution, e.g., $P(\mathcal{D}) = \sum_k P(\mathcal{D}|k)P(k)$, which incorporates the prior distribution and likelihood functions for all classes. In Grau et al. (2004), authors define two prior distributions: (1) a spatial prior that encourages neighboring voxels to share the same label, and (2) an intensity prior for each pixel in the image obtained by registering an image atlas to the recorded image. Their results demonstrate that application of prior information in this way can both address the shortcomings found in prior implementations of the watershed

transform for segmentation and compute highly accurate solutions to very difficult segmentation problems. However, there has been little work to date to extend this framework to other MRI segmentation problems or to other medical imaging modalities. The main impediments to broadening the application of this framework is determining the appropriate prior models to apply. For bone fragment segmentation problem, the prior information is not available due to the large variation and randomnicity in fragments characteristics such as shape, position, orientation, and texture. So, the improved watershed algorithm dependency on prior information is not desirable.

## 3. Methodology: Bone Fragment Segmentation Using the PWT Algorithm

The bone fragment segmentation algorithm uses the PWT algorithm to extract bone fragment regions from a CT image. The proposed algorithm seeks to address two issues: (1) how to accurately segment bone fragments that touch, i.e., are in close proximity to one another, and (2) how to accurately segment bone fragment tissue from other tissues. It does this by developing probabilistic models for both situations and then integrating these models into a single probabilistically-driven version of the classical watershed transform, referred to as the PWT.

The bone fragment segmentation algorithm takes as input a CT image of the limb ($I$) and a set of user settings. The output of this algorithm is a labeled image where each unique label corresponds to a unique bone fragment. The algorithm consists of three steps:

1. Classify the input image pixels into three sets: non-bone, cortical bone, and non-cortical bone,
2. Compute probability distributions,
3. Perform the PWT algorithm.

These steps are shown in figure (4). By performing these steps, an estimate of bone fragment regions in a CT image is obtained. This algorithm processes the entire image at once for both 2D image and volumetric 3D ones.

Two user settings specify the parametric information needed to run the bone fragment segmentation algorithm. This unknown information include: (1) the maximum size in pixels of false positive markers, referred to as size threshold ,$T_{size}$, and (2) the maximum background-to-bone pixel distance which is used to mark pixels considered to be in narrow "isthmus" in regions.

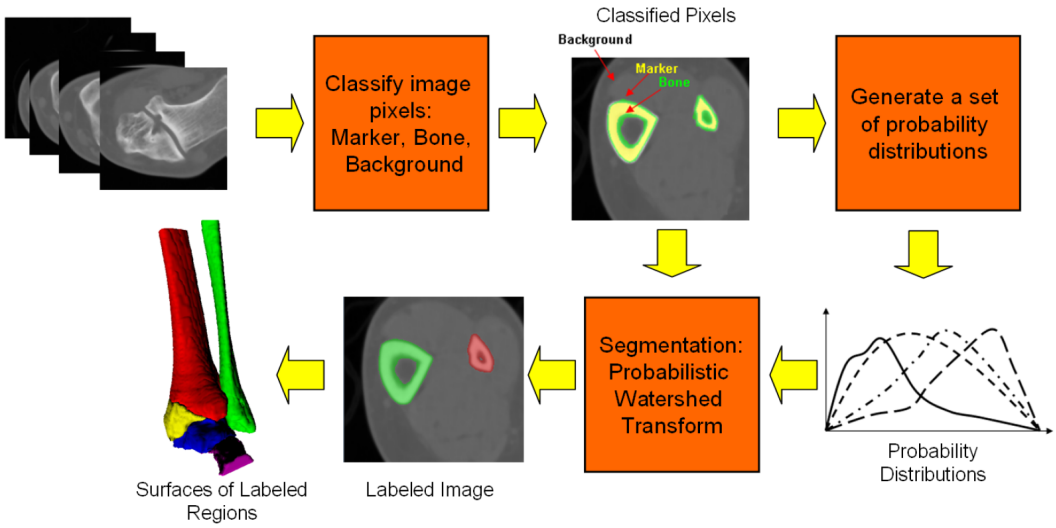


Figure 4: Shows the three steps to perform the bone fragment segmentation algorithm: (1) Classify the input image pixels into three sets: markers, data, and background, (2) Compute class-conditional probabilistic reliefs, and (3) Compute watershed to expand the image markers in the order of slowest cost ascent until all non-markers pixels belong to some marker.

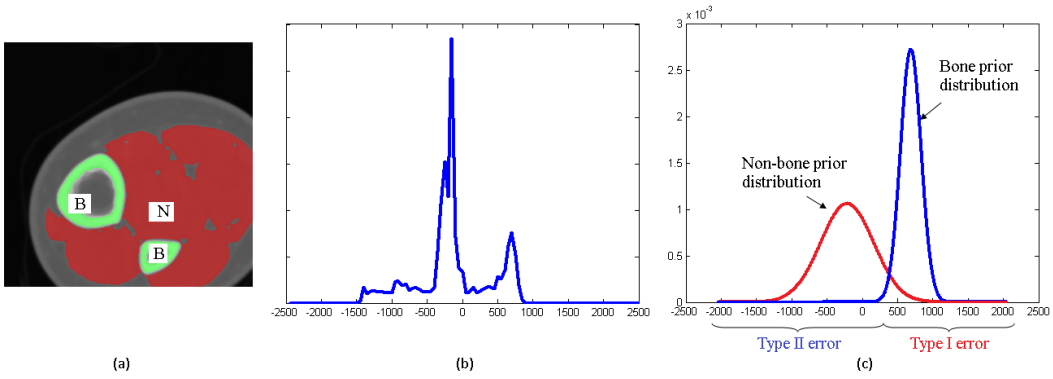


Figure 5: (a-c) show how a pair of prior distributions are used to estimate the bone tissue pixels in a CT image. (a) shows an example for a CT image segmented into bone tissue, denoted B, and non-bone tissue, denoted N, are manually segmented. (b) shows the histogram of pixel intensities for the segmented bone and non-bone areas. (c) shows the pair of Gaussian prior distributions for bone, and non-bone tissues

### *3.1. Image Pixel Classification*

Pixel classification is the first step in bone fragment segmentation algorithm. This step takes three inputs: (1) the CT image $I$, and (3) the size threshold $T_{size}$. The outputs of this step are: (1) a collection of pixel regions called markers, $\mathbf{M}$, (2) a set of non-cortical bone tissue pixels, $D$, and (3) a set of background pixels, $BG$. This is accomplished via a two-stage classification process. Stage 1 classifies the image pixels as bone tissue or non-bone (background) tissue. Stage 2 sub-divides the bone tissue into cortical bone tissue and non-cortical bone tissue. The three tissue classes are computed using two intensity threshold values: (1) cortex, $T_{cortex}$, and (2) bone, $T_{bone}$. Threshold values are estimated using a prior distribution for bone tissue, $p(w_{bone})$, in CT images, where $w_{bone}$ denotes the class for the bone region. Figure (5) shows the generated prior distribution as a function of CT intensity for bone tissue within the human body as well as a prior distribution for non-bone tissue. The prior distributions are approximated by two Gaussian functions, one for bone tissue and the second non-bone tissue. Image data shown in the results section, were segmented with priors having means of the bone tissue and non-bone tissue distributions were 692 and -212, respectively. The CT values in the image are represented by 12-bit numbers range from -2048 to 2047. These findings are consistent with CT values reported for human

bone and soft tissues as reported in Feeman (2009). Automated algorithms other than global threshold to estimate the three regions, i.e., non-bone region, non-cortical bone region and cortical bone region, are reported in Aslan et al. (2009); Janc et al. (2011). Adjustments to this approach may be required with distinct imaging machinery due to intensity and scale variations that can exist for different CT imaging manufacturers.

The first classification stage applies a global threshold, $T_{bone}$, to classify image pixels into bone pixels or background pixels. Bone pixels are those pixels having intensity greater than or equal to the bone threshold, i.e., $X_{bone} = \{\mathbf{x}|I(\mathbf{x}) \geq T_{bone}\}$ where $I(\mathbf{x})$ is the image intensity for pixel at location $\mathbf{x}$. all other pixels are classified as background pixels, i.e., $BG = \overline{X}_{bone}$.

The bone threshold $T_{bone}$ value is specified by finding the intersection point between bone prior and non-bone prior distribution. In order to minimize Type 2, i.e., reduce false non-bone tissue pixels classification, $p(w_{bone})$ is multiplied by a constant that is $> 1$ to shift the threshold to lower probabilities of $p(w_{bone})$. For the results shown, this constant was set to 100 which is the bone threshold, i.e., $T_{bone}$= 180. Users may change the constant values as appropriate to fit the imaging devices used in their application, e.g., using the standardized range for Hounsfield units that the cortex and cancellous tissues occupy.

The second classification stage applies a global threshold, $T_{cortex}$, to classify bone pixels $X_{bone}$ into cortical bone pixels or non-cortical bone pixels. Cortical bone pixels are those pixels having an intensity greater than or equal to the cortical bone threshold , i.e., $X_{cortex} = \{\mathbf{x}|I(\mathbf{x}) \geq T_{cortex}, \mathbf{x} \in X_{bone}\}$. all other bone pixels are classified as non-cortical bone pixels, i.e., $D = X_{bone} \cap \overline{X}_{cortex}$.

The cortical bone threshold $T_{cortex}$ is determined using the prior distribution for bone tissue, $p(w_{bone})$. The value of $T_{cortex}$ is specified by finding the other intersection point between bone prior and non-bone prior distributions, which is to the right of the bone prior distribution's center. In order to minimize Type 1, $p(w_{bone})$ is multiplied by a constant that is $< 1$ to shift the threshold to higher probabilities of $p(w_{bone})$. In this work, the constant is set to 0.05 so that the intersection point is approximated to 600HU which is the cortical bone threshold, i.e., $T_{cortex}$= 600. Users may change the constant value as appropriate to fit the imaging devices used in their application.

The set of cortex pixels $X_{cortex}$ is decomposed into a disjoint union of marker regions, i.e., $X_{cortex} = \bigcup_i M_i$, where $M_i$ is the $i^{th}$ marker. Markers are intended to be a coarse labeling of the final segmented image. Each

marker will ultimately define a distinct PWT region having a unique label. Hence, the number of provided markers is also the estimated number of bone fragments in the image.

Markers having volume less than the user-specified minimum size, $T_{size}$ are removed resulting in a collection of marker regions referred to as $\mathbf{M}$, i.e., $\mathbf{M} = \{M_i, |M_i| \geq T_{size}, M_i \in X_{cortex}\}$ where $|M_i|$ denotes the number of pixels in $M_i$. This process filters out bone fragment detections due impulse noise and detections corresponding to clinically irrelevant (small) bone fragments. Pixels associated with removed markers are added to the set of non-cortical bone pixels

### *3.2. Probability Distributions Computation*

The second step of the bone fragment segmentation algorithm takes five inputs: (1) the CT image $I$, (2) the set of markers $\mathbf{M}$, (3) the set of bone pixels $D$, (4) the set of background pixels $BG$, and (5) the maximum pixel-to-background distance observed among all detected "isthmus" pixels $d_{max}$, and provides as output K class-conditional likelihood functions; one for each detected marker, where K is the number of detected markers. The likelihood functions define the stochastic relationship between the each unclassified, i.e., non-marker, bone pixel and each of the markers. Let $f_k(\mathbf{x})$ denote the $k^{th}$ likelihood function evaluated at pixel location $\mathbf{x}$ whose value is the likelihood that the intensity $I(\mathbf{x})$ is a measurement from the $k^{th}$ bone fragment, or equivalently, that the pixel at $\mathbf{x}$ is from class $w_k$.

Two pixel likelihoods are used to form the likelihood function $f_k(\mathbf{x})$: (1) a pixel-to-fragment model and (2) an "isthmus" model. An "isthmus" indicator function, $\mathbf{1}_{isthmus}(\mathbf{x})$, is used to select one of these two models at each image location.

*Pixel-to-Fragment Probabilities*

Pixel-to-fragment probability computation class-conditional likelihood functions model the likelihood of a pixel based on its spatial proximity and intensity similarity to a candidate fragment.

The total likelihood is taken as the product of two likelihoods: 1) a position-to-marker based likelihood and 2) intensity-to-maker likelihood. The position-based and intensity-based likelihoods are assumed to be conditionally independent. The fragment probability distribution is computed in equation (1):

$$p(w_k|I(\mathbf{x}),\mathbf{x},k,\mathbf{M}) = \frac{p(w_{frag_k}|I(\mathbf{x}),k,\mathbf{M})\,p(w_{frag_k}|\mathbf{x},k,\mathbf{M})}{p(I(\mathbf{x}),\mathbf{x},\mathbf{M})} \tag{1}$$

where $p(w_k|I(\mathbf{x}),\mathbf{x},k,\mathbf{M})$ is the posterior pixel-to-fragment probability for pixel at location $\mathbf{x}$ to have come from the $k^{th}$ fragment/marker. It is comprised of the product of $p(w_k|I(\mathbf{x}),k,\mathbf{M})$, the likelihood of observed intensity, $I(\mathbf{x})$,to come from the $k^{th}$ marker and $p(w_k|\mathbf{x},k,\mathbf{M})$ the likelihood of position $\mathbf{x}$ to be a member of the $k^{th}$ marker. The normalization $p(I(\mathbf{x}),\mathbf{x},\mathbf{M}) = \sum_k p(w_k|I(\mathbf{x}),\mathbf{x},k,\mathbf{M})$ corresponds to the evidence term in typical Bayesian classification and normalizes the product to be a well-defined probability distribution. In practice, posterior probabilities need only be computed for bone pixels only, i.e., $\mathbf{x} \in D$. The computation of probability distribution is based on spatial and intensity information that are obtained from inside the image to reduce heterogeneity. Intensity distribution inside the bone region may vary significantly from one dataset to another depending on the parameters of acquisition, the imaged body part, and the nature of the bone tissue for a patient.

The position-to-marker likelihood, $p(w_k|\mathbf{x},k,\mathbf{M})$, is computed as the ratio of the reciprocal of the closest distance between point $\mathbf{x}$ and the boundary of marker $M_k$ for the $k^{th}$ bone fragment to the sum of the reciprocals of the individual closest distances between point $\mathbf{x}$ and all marker boundaries. The computation of $p(w_k|\mathbf{x},k,\mathbf{M})$ is shown in equation (2).

$$p(w_k|\mathbf{x},k,\mathbf{M}) = \frac{\frac{1}{dist(\mathbf{x},M_k)}}{\sum_{i=1}^{K}\frac{1}{dist(\mathbf{x},M_i)}} \tag{2}$$

where $dist(\mathbf{x},M_i)$ is the shortest 3D Euclidean distance between pixel $\mathbf{x}$ in the image and the boundary marker region $M_i$; see figure (6) for a graphical explanation and equation (3) for the mathematical definition

$$dist(\mathbf{x},M_i) = \min_{\forall \mathbf{x_j} \in M_i}\{||\mathbf{x}-\mathbf{x_j}||\} \tag{3}$$

where $\|\cdot\|$denotes the 3D Euclidean distance. The computation of the position likelihood is based on the assumption that a bone pixel is most likely part of the bone fragment region which has the closest cortical pixels to that bone pixel. This assumption is based on the fact that bone structures are continuous, smooth and covered by cortical tissue (the envelope assumption). The position-based likelihood serves as a shape based probability for each bone fragment class.

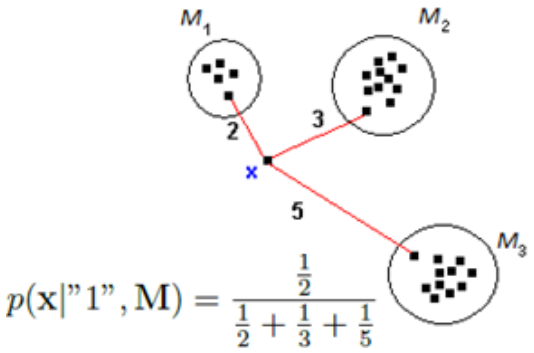


Figure 6: An example of how to compute the position likelihood for pixel $\mathbf{x}$ given the first marker and the set of markers $\mathbf{M} = \{M_1, M_2, M_3\}$. $p(\mathbf{x}|"1", \mathbf{M})$ is the ratio of the reciprocal of the distance between point $\mathbf{x}$ and marker $M_1$ to the sum of the reciprocals of the individual distances between point $\mathbf{x}$ and all markers, refer to equation (2).

The intensity-to-marker likelihood, $p(w_k|I(\mathbf{x}), k, \mathbf{M})$ is modeled via a Laplace distribution as shown in equation (4).

$$p(w_k|I(\mathbf{x}), k, \mathbf{M}) = \frac{1}{2}\exp(-|I(\mathbf{x}) - \mu_k(\mathbf{x})|) \tag{4}$$

where $\mu_k(\mathbf{x})$ is the location parameter of the Laplace distribution. The computation of intensity likelihood is based on the assumption that bone structures typically exhibit an exponential decaying of intensity in CT images from their cortex. $\mu_k(\mathbf{x})$ is computed using equation (5):

$$\mu_k(\mathbf{x}) = \frac{1}{|LS(d)|}\sum_{\mathbf{x}_i \in LS(d)} I(\mathbf{x}_i) \tag{5}$$

where $d$ is the closest 3D distance between pixel $\mathbf{x}$ and the boundary of the $k^{th}$ marker $M_k$, i.e., $d = dist(\mathbf{x}, M_k)$ and $LS(d)$ is the set of unclassified bone pixels that are equi-distant to their closest marker, i.e., those pixels that satisfying $dist(\mathbf{x}_i, \mathbf{M}) - d = 0$. $LS(d)$ is computed as in equation (6).

$$LS(d) = \{\mathbf{x}_i | dist(\mathbf{x}_i, \mathbf{M}) - d = 0, \forall x_i \in D\} \tag{6}$$

The distance between a pixel $\mathbf{x}_i$ and the set of markers $\mathbf{M}$, i.e., $dist(\mathbf{x}_i, \mathbf{M})$, is calculated similarly to equation (3) but differs in that it considers all unclassified bone pixels, $\mathbf{x}_i$, and markers as shown in equation (7):

$$dist(\mathbf{x}_i, \mathbf{M}) = \min_{\forall \mathbf{x_j} \in \mathbf{M}} ||\mathbf{x}_i - \mathbf{x_j}|| \tag{7}$$

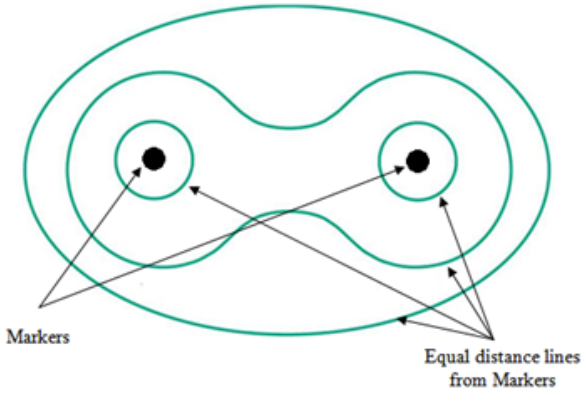


Figure 7: An illustration picture to show the equal distance lines from markers. Along each line, pixels are assumed to have the same intensity value.

The computation of $\mu_k(\mathbf{x})$ is based on the assumption that the intensity values decay similarly a a function of distance from the marker boundary for all fragment. Hence, unclassified bone pixels having identical pixel-to-fragment distances are expected to have the same intensity value, see figure (7) . This assumption is based on the fact that bones exhibit smooth structural changes and will have similar trabecular structure as a function of distance from the bone cortex.

The normalization factor, $p(I(\mathbf{x}), \mathbf{x}, \mathbf{M})$, ensures that the likelihood probability in the left-hand side of equation (1) is a valid probability which sums over all possible hypotheses to one. This normalization factor is computed in equation (8):

$$p(I(\mathbf{x}), \mathbf{x}, \mathbf{M}) = \sum_{k=1}^{K} p(w_k | I(\mathbf{x}), k, \mathbf{M})\, p(w_k | \mathbf{x}, k, \mathbf{M}) \tag{8}$$

where $K$ is the number of markers.

*Isthmus Probabilities*

A second "isthmus" class-conditional likelihood function is purpose-built to segment the difficult decision regions where island-like (hence "isthmus") groups of bone pixels are found distant from marker/cortex regions. These pixels typically correspond to fractured trabecular tissue surrounded by multiple touching bone fragment regions. The isthmus likelihood serves to segment these pixels as a post-processing step a custom model are not classified by the a fore-mentioned pixel-to-fragment likelihood.

Given the high uncertainty of the label of these pixels, we impose a likelihood on these pixels that is independent of the fragment regions and observed intensity. Specifically, we assign these pixels the one-sided triangular distribution based on their distance to the nearest background pixel as shown in equation (9):

$$p_{isthmus}(\mathbf{x}|\mathbf{M}, BG, d_{max}) = \begin{cases} \frac{2}{d_{max}^2}(d_{max} - dist(\mathbf{x}, BG)) & for \quad dist(\mathbf{x}, BG) \leq d_{max} \\ 0 & otherwise \end{cases} \tag{9}$$

This has the effect of assigning highest probabilities to the unclassified isthmus pixels farthest from the background and decreasing probabilities to those isthmus pixels that lie closer to background (typically soft tissue) pixels. The value $d_{max}$ is the maximum pixel-to-background distance observed among all detected "isthmus" pixels. Note that the pixel-to-background distance is defined as the length of the shortest path that connects an "isthmus" bone pixel to a background pixel such that this path does not include any marker pixel. Computation of distances for pixels-to-background path is accomplished using the wavefront propagation algorithm described in Porikli and Kocak (2007).

*Combined Probabilities for PWT Computation*

The pixel-to-fragment and isthmus probabilities are merged to generate a set of probability distributions $\{f_k\}$ that represent the likelihood that the measurement at position $\mathbf{x}$ is a member of the $k^{th}$bone fragment (or equivalently class $w_k$).

An indicator function is used to mark those pixels lying at "isthmus" locations and is used to mathematically switch between pixel-to-fragment and "isthmus" probabilities. Isthmus pixels are detected based on their pixel-to-background distance as indicated in equation (10).

$$\mathbf{1}_{isthmus}(\mathbf{x}) = \begin{cases} 0, & dist(\mathbf{x}, BG) < d_{max} \\ 1, & otherwise \end{cases} \tag{10}$$

The indicator function has the impact of marking pixels that are either (1) distant from a marker or (2) close to the background as candidate "isthmus" locations. These particularly challenging regions are assigned the lowest likelihood function values. As such, they will be visited last using the PWT algorithm which adopts a highest-likelihood-first region growing procedure.

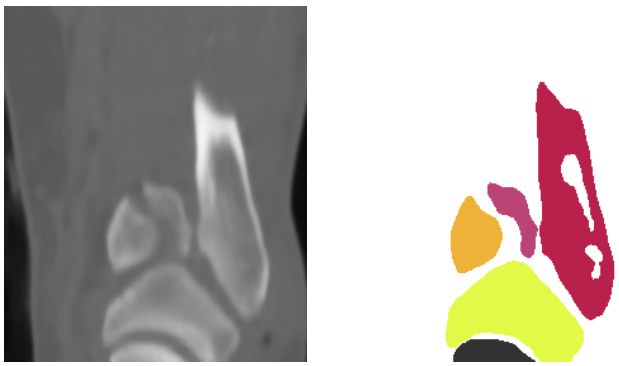

(a) (b)

Figure 8: Bone fragment segmentation result using the PWT algorithm, (a) original image, (b) segmentation results, each unique label is represented with a unique color. The white area represents the background points in $BG$.

The PWT probability distributions are computed in equation (11):

$$f_k(\mathbf{x}) = \begin{cases} p(w_k|I(\mathbf{x}), \mathbf{x}, k, \mathbf{M}) + \max_{\mathbf{x}} p_{isthmus}(\mathbf{x}|\mathbf{M}, BG, d_{max}) & if \quad \mathbf{1}_{isthmus}(\mathbf{x}) = 0 \\ p_{isthmus}(\mathbf{x}|\mathbf{M}, BG, d_{max}) & if \quad \mathbf{1}_{isthmus}(\mathbf{x}) = 1 \end{cases} \tag{11}$$

where $f_k(\mathbf{x})$ is the likelihood function associated with marker $M_k$ for pixel $\mathbf{x}$. The algorithm uses $\mathbf{1}_{isthmus}(\mathbf{x})$ to switch between pixel-to-fragment and "isthmus" probability models. Adding $\max_{\mathbf{x}} p_{isthmus}(\mathbf{x}|\mathbf{M}, BG)$ to the pixel-to-fragment probability shifts the likelihood function values for all non-isthmus pixels to ensure they are segmented prior to segmenting any "isthmus" pixels in the PWT algorithm.

### *3.3. Performing the PWT Algorithm*

Performing the PWT algorithm is the fourth step of the bone fragment segmentation algorithm. This step takes four inputs: (1) the set of markers $\mathbf{M}$, (2) the set of bone pixels $D$, (3) the set of background pixels $BG$, and (4) the set of probability distributions $\{f_k\}$. The output of this step is a collection of labels, one for each bone pixel. The collection of bone pixels that share the same label form a unique segment which represents a unique bone fragment in the image, see figure (8).

The PWT algorithm is performed as described in Shadid and Willis (2013). The algorithm starts by assigning a unique label for each marker

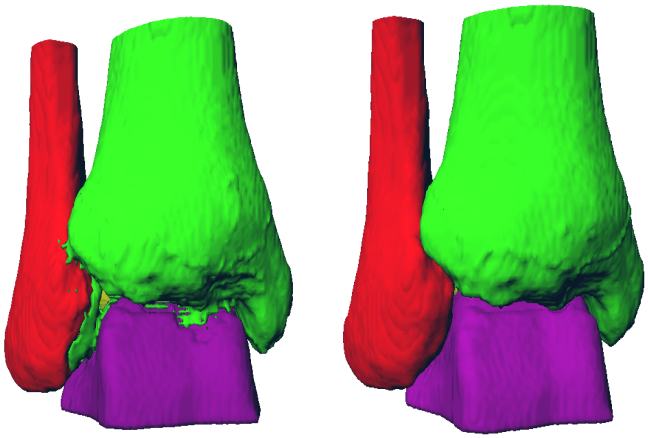

(a) (b)

Figure 9: (a,b) shows a segmentation result excluding (a) and including(b) the use of "isthmus" probabilities. Note that inclusion of these probabilities allows some parts of the fibula and talus segmentation to be corrected.

and label its pixels with the same label. Then, the labels of the markers are expanded into bone pixels according to their probability distributions. Pixels with higher probability values are processed before pixels with lower probability values. Once the PWT algorithm finishes its operations, the collection of the labeled pixels represent the estimated bone fragments in the image and the background set $BG$ contains the pixels that do not belong to any bone fragment.

The PWT algorithm assigns labels to non-"isthmus" pixels before assigning labels to "isthmus" pixels because none "isthmus" pixels have higher probabilities. This order of assignment reduces the expansion of any incorrect labels for pixels in the narrow bone areas to none "isthmus" pixels. For "isthmus" pixels, the PWT algorithm expands labels by adding an additional layer of pixels neighboring those already labeled ones at each step, starting from the farthest pixels from the boundary of the bone region since they have higher probabilities, refer to equation (11). This order of assignment causes "isthmus" pixels to be divided evenly between neighboring segments. Figure (9) shows an example of segmentation results with and without the use of "isthmus" probabilities demonstrating their role for correctly labeling difficult bone fragment pixels.

## 4. Results

The bone fragment segmentation algorithm was quantitatively evaluated to better understand the strengths and weaknesses of this algorithm. The quantitative evaluation is performed over 2D images and 3D images. For 2D images, the evaluation is performed by comparing results from a collection of segmentation algorithms, including results from the proposed algorithm, with results established as the ground truth. Analysis proceeds by studying the geometric properties of the segmentation boundaries and regions for a select group of interesting images. For 3D images, the experiment compares segmentations for the PWT algorithm with the ground truth examples provided by the work in Liu (2012a). The ground truth examples are surfaces for tibia fragments generated by triangulating segments that have been manually generated by a human. The comparison process generates surfaces for the segments generated by the PWT algorithm. Then, it computes the evaluation metric that measures the segmentation difference by comparing the boundaries of the two surfaces using a boundary difference score.

The clinical data set includes six cases for tibia fractures where each case includes an image of a broken limb and an image of an unbroken limb. These fracture cases range from low energy fracture events such as 1.5 foot fall, to high energy fracture events such as a 50 mph car accident. The images are 3D CT scans in DICOM format and 16-bit are used to express the CT numbers. Each volume contains of 81 to 302 contiguous axial slices with a slice thickness of 5mm. 2D images are generated by selecting slices from the 3D scans from axial, sagittal, and coronal view perspectives to represent normal and abnormal cases of intact and fractured shapes of bone fragments.

The proposed segmentation algorithm evaluation approach requires a definition of a ground truth segmentation for each image. The ground truth segmentation is generated by employing a human to manually segment each image. The set of human generated segmentations were taken as a collection of "ground truth" examples. The segmentation algorithm is then quantitatively evaluated by comparing its result with the ground truth examples. The evaluation approach uses region based metrics and a boundary based one to know how well the segmentation algorithm performs. The region based metrics include: 1) accuracy, 2) sensitivity, 3) specificity, 4) overlap, 5) precision, 6) recall, 7) $F_1$ score, 8) Hamming distance, and 9) Region Rank (RR). While the used boundary based metric is Cut Discrepancy (CD). These metrics are taken from Barrett and Swindell (1996); Powers (2007); Mookiah

et al. (2013); Chen et al. (2009); Shadid and Willis (2013). The performance of the PWT segmentation algorithm is compared with several algorithms used for bone segmentation to show how well it performs with respect to them.

### *4.1. Evaluation Results and Discussion*

A comparative evaluations experiment was conducted to evaluate the performance of the bone fragment segmentation algorithm on 2D images and 3D images. For 2D images, The evaluation compares the bone fragment segmentation algorithm using the PWT algorithm, referred to as the PWT algorithm for abbreviation, with the most competing segmentation algorithms found in Shadid and Willis (2013): Threshold, Otsu (1979), and Watershed, Meyer (1991). The threshold technique is implemented using Otsu's algorithm in MATLAB. It takes as input a 2D image and provides as output closed contours for the segmented regions where each enclosed region represents a unique segment. The dark background region in the input image is excluded from the threshold calculations to avoid segmenting the whole limb. The watershed technique is implemented using Meyer's algorithm in MATLAB. It takes as input a 2D image that is a modified version of the CT one such that it includes the estimated bone region and has minima at the estimated cortical regions, only . These cortical and bone regions are the same ones used in the PWT algorithm. Level set and active contour techniques are ignored in this comparison, because they are more suitable for segmenting one target component object, e.g., intact bone, than several bone segments as indicated in Shadid and Willis (2013). The variation of intensity in texture areas generates strong internal forces within bone regions that affect deformable models. These internal forces move the initial contours for deformable models toward regions boundaries making a deformation process to split internal structures and textures of bone regions.

Figure (10), shows image segmentation result for a 2D CT image of a fractured bone using seven different image segmentation methods. This figure is presented to allow for visual comparison of the results and to better understand the strengths and weaknesses of the PWT algorithm. The PWT settings that are used to segment the image are: $T_{size} = 15$ pixel, and $d_{max} = 15$ pixel. The result suggests that the PWT algorithm can generate similar segmentation results to the ground truth examples.

The segmentation algorithms used in the test generated different results when they applied on CT images of a fractured bone. The proposed algo-

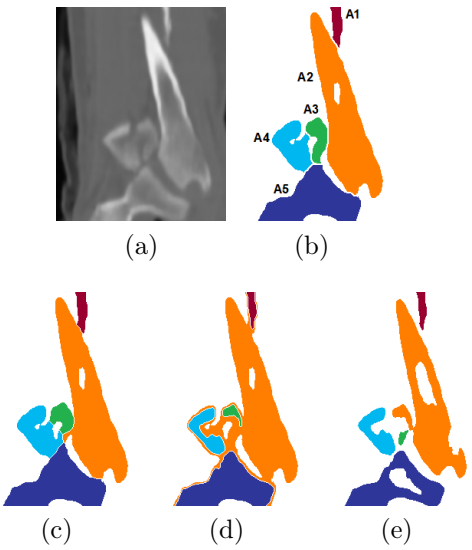


Figure 10: Image segmentation results for a 2D CT sagittal slice image of a fractured ankle with severity score 58 using four different segmentation methods. (a) The input image. (b-e) The segmentation results generated by the used segmentation methods: (b) humans ("ground truth"), (c) the PWT algorithm, (d) the watershed algorithm , and (e) the threshold algorithm.

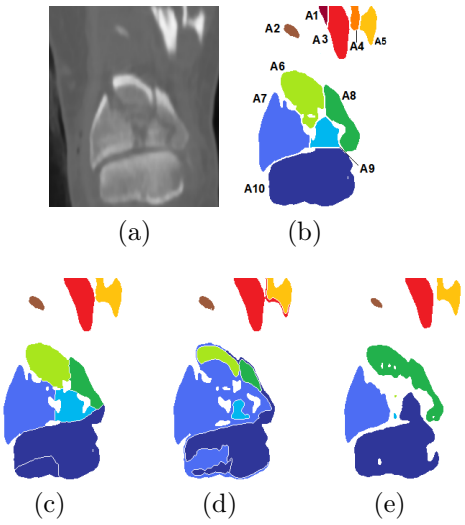


Figure 11: Image segmentation results for a 2D CT coronal slice image a fractured ankle with severity score 71 using four different segmentation methods. (a) The input image. (b-e) The segmentation results generated by the used segmentation methods: (b) humans ("ground truth"), (c) the PWT algorithm, (d) the watershed algorithm , and (e) the threshold algorithm.

rithm was able to segment bone fragments. Also, it did not show a leak problem through areas of close proximity. The watershed algorithm was able to generate the correct number of fragments but it suffers a lot from the leak problem. It did not stop at the boundaries of bone fragments and kept growing segments specially through close proximity areas, e.g., fragment $A_2$ is kept growing into regions of other fragments and not stopped at its boundaries. The thresholding algorithm was not able to separate bone fragments in close proximity, e.g., fragments $A_2$ and $A_3$ are wrongly joined together. In addition, it was not able to segment all cancellous tissue.

The compared segmentation algorithms are applied to other datasets of fracture cases to generalize the result, for example see figures (11 and 12). Figure (12) shows the importance of the fragment probability which depends on the position and intensity information of the pixels. The PWT segmentation result for fragments A2 and A4 are closer to the ground truth than any other segmentation algorithm. That is because the separating pixels between these fragments have intensities lower than expected by the Laplace

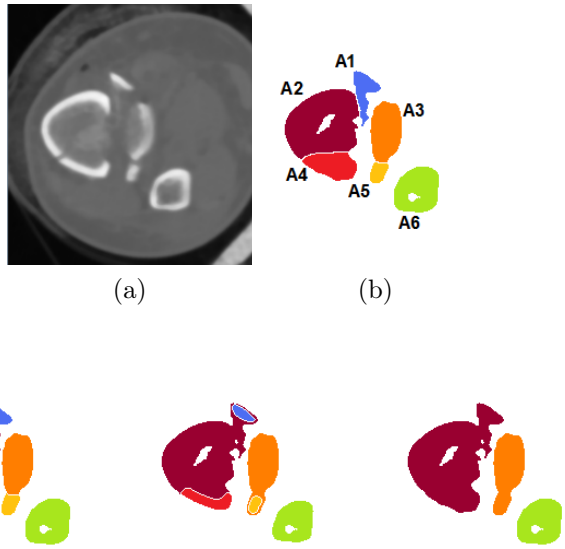


(a) (b)

(c) (d) (e)

Figure 12: Image segmentation results for a 2D CT sagittal slice image of a fractured ankle with severity score 74 using four different segmentation methods. (a) The input image. (b-e) The segmentation results generated by the used segmentation methods: (b) humans ("ground truth"), (c) the PWT algorithm, (d) the watershed algorithm , and (e) the threshold algorithm.

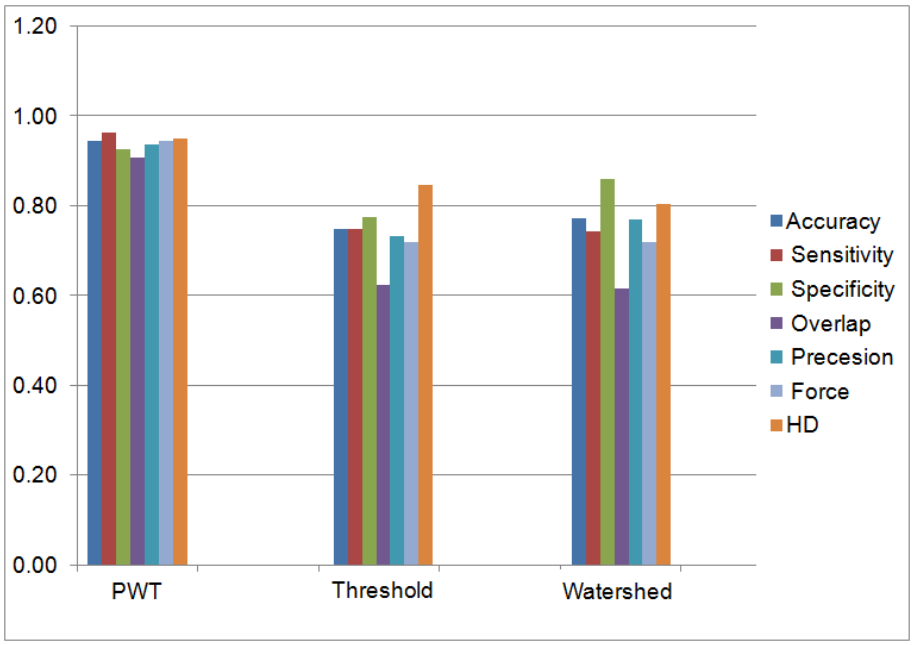


Figure 13: A chart for region based evaluation scores for segmentation results of all 2D images. The x-axis represents the region based metrics for different segmentation algorithms while the y-axis represents the measured metric value.

distribution. So low probability values are generated for them in order to be processed last by the PWT algorithm. The segmentation results of different algorithms are quantitatively evaluated. Figure (13) shows a bar chart of the evaluation scores for the six automatic segmentation methods when evaluated over all the images. There are seven unique region based evaluation metrics that are reported: 1) accuracy, 2) sensitivity (recall), 3) specificity, 4) overlap, 5) precision, 6) $F_1$ score, and 7) HD. Table (1) shows the measured seven region based metrics. The average of all region based metric is computed to rank segmentation algorithms. This average is referred to as a Region Rank metric (RR). The RR metric for segmentation algorithms is reported separately in a table and a chart. Figure (14) shows a chart of the RR metric while table (2) shows the RR metric for segmentation algorithms. The PWT segmentation has the score closest to the score for the ground truth examples among all the automatic segmentation algorithms. This indicates that the regions computed by the PWT algorithm are close

| Method | Accuracy | Sensitivity | Specificity | Overlap | Precision | $F_1$ | HD |
|---|---|---|---|---|---|---|---|
| Threshold | .75±.1 | .75±.08 | .78±.15 | .62±.14 | .73±.19 | .72±.13 | .85±.06 |
| Watershed | .77±.2 | .74±.23 | .86±.16 | .62±.2 | .77±.15 | .72±.19 | .80±.07 |
| PWT | .94±.04 | .96±.03 | .93±.05 | .91±.06 | .94±.04 | .94±.04 | .95±.03 |

Table 1: Region based evaluation scores for segmentation results of all 2D images computed for the different segmentation algorithms used in performance comparison. All metrics values range from 0 to 1. The smaller the degree of mismatch, the closer the metric value to 1. The values are reported using the following format: $\mu \pm \sigma$, where $\mu$ is the average score and $\sigma$ is the standard deviation.

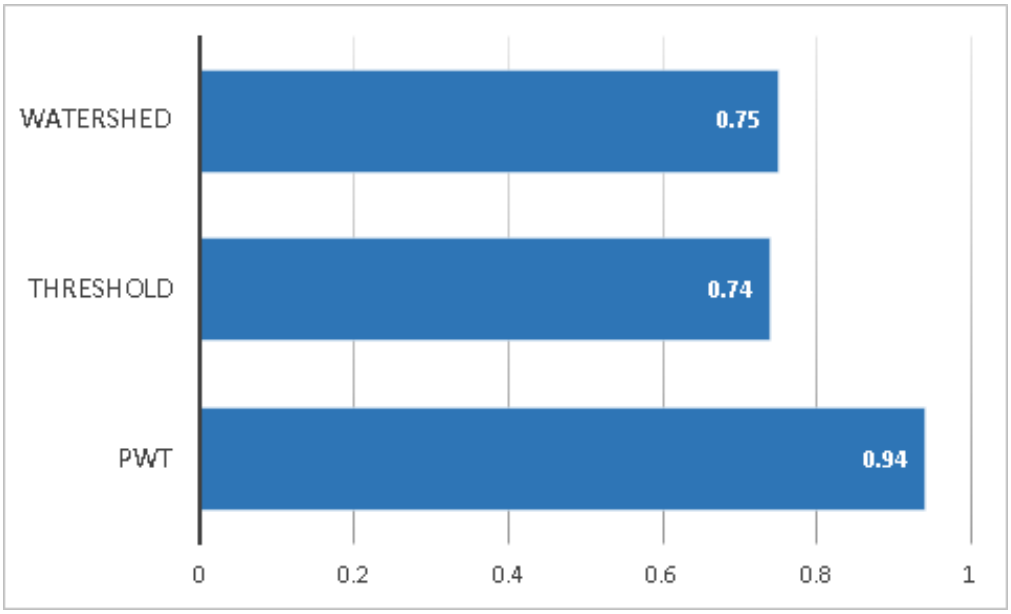


Figure 14: A chart for RR evaluation score for segmentation results of all 2D images to compare the performance of the different segmentation algorithms.

| Method | Threshold | Watershed | PWT |
|---|---|---|---|
| RR | 0.74±.12 | 0.75±.17 | 0.94±.04 |

Table 2: RR evaluation score for segmentation results of all 2D images computed for the different segmentation algorithms used in performance comparison. The metric value ranges from 0 to 1. The smaller the degree of mismatch, the closer the metric value to 1. The values are reported using the following format: $\mu \pm \sigma$, where $\mu$ is the average score and $\sigma$ is the standard deviation.

| Method | Threshold | Watershed | PWT |
|---|---|---|---|
| CD | 0.13±.08 | 0.28±.12 | 0.03±.02 |

Table 3: CD evaluation score for segmentation results of all 2D images computed for the different segmentation algorithms used in performance comparison. Metric values range from 0 to 1, the smaller the degree of mismatch, the closer the metric value to 0. The values are reported using the following format: $\mu \pm \sigma$, where $\mu$ is the average score and $\sigma$ is the standard deviation.

to the regions specified in the ground truth segmentations. The boundary based comparison metric CD for segmentation algorithms is reported in a table and a chart. Figure (15) shows a chart of the CD metric while table (3) shows the CD metric for segmentation algorithms. For this metric, the PWT segmentation has the score closest to the score for the ground truth examples among all the automatic segmentation algorithms. This indicates that the shapes of the regions computed by the PWT algorithm are close to the shapes of the regions specified in the ground truth segmentations. The small value of the computed CD metric for the PWT algorithm indicates that the PWT algorithm will not over-segment or under-segment most of models in the dataset. Hence, all evaluation scores indicate that the PWT algorithm tends to produce good segmentations when evaluated over all the 2D images in the test dataset.

The PWT algorithm typically out-perform the analyzed competing segmentation methods. This can be explained for three main reasons: 1) the use of unmodified intensity information in the computation of pixel-to-fragment probabilities, 2) the use of distance information between pixels and markers in the computation of pixel-to-fragment probabilities, and 3) the use of "isthmus" probabilities to enhance the segmentation result in "isthmus" bone

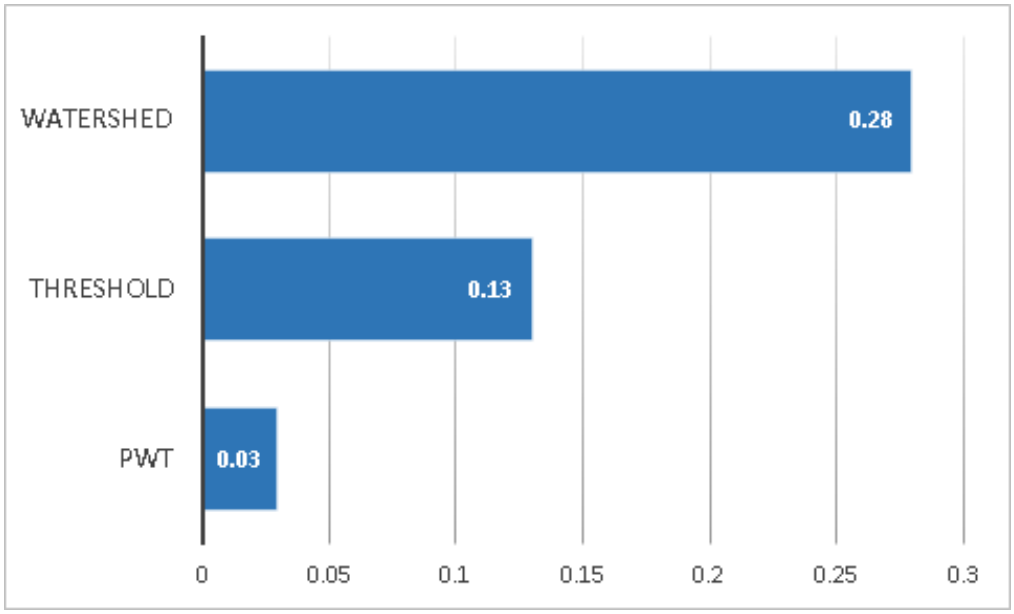


Figure 15: A chart for CD evaluation score for segmentation results of all 2D images to compare the performance of the different segmentation algorithms.

regions. Figure (16) shows an example of how the use of "isthmus" probabilities reduces the leak problem in 2D and 3D. Figures (16 b and c) demonstrate the improvement in segmentation results in 2D due to the use of "isthmus" probabilities. The leak may appear in small in 2D but when it continues in 3D across other slices the problem grows up and cross multiple bone as shown in figure (16 d). In figure (16 d) parts of the talus (purple) marked as tibia (green) and some of them are located away from where the leak started. Figure (16 e) demonstrates the capability of "isthmus" probabilities to enhance the segmentation result and reduce the leak problem.

The performance of the PWT bone fragment segmentation algorithm is quantitatively evaluated on 3D CT images. The performance is evaluated by applying the PWT algorithm on two 3D CT images of ankles to segment the tibia: one image for an unbroken tibia and a second records a fractured tibia after an injury. This evaluation is conducted on unbroken bone and a fractured one to prove that the proposed algorithm is not limited to fractured bones only. The estimated surfaces by the algorithm are compared to ground truth surfaces provided by the work in *Liu (2012b)*. The estimated surfaces are extracted from the volume data using the marching cubes algorithm

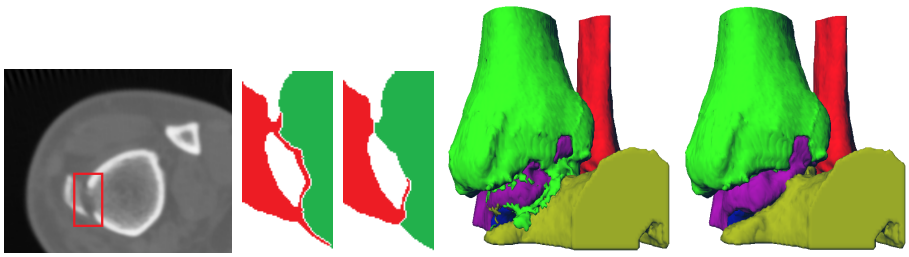

(a) (b) (c) (d) (e)

Figure 16: An example shows the enhancement benefit of "isthmus" probabilities in 2D and 3D images of left ankle. (a) is the input image. (b) is the segmentation results using the pixel-to-fragment probabilities only. (c) is the segmentation result using the combined pixel-to-fragment probabilities and "isthmus" probabilities. (d) The 3D segmentation results using the pixel-to-fragment probabilities only. (e) The 3D segmentation result using the pixel-to-fragment probabilities and "isthmus" probabilities.

described in Hansen and Johnson (2005). The performance is measured by computing the cut discrepancy metric which evaluates average distance between the points of the estimated surfaces and their corresponding points in the ground truth surfaces.

Figure (17) shows a segmentation result for a 3D CT image for unbroken tibia using the PWT algorithm. The images show the segmentation result of the PWT algorithm for the tibia bone (in red) together with its "ground truth" segmentation (in pink) from three different view perspectives: axial, coronal, and sagittal. They are shown together to allow for visual comparison of the results and to better understand the strengths and weaknesses of the PWT algorithm. The "ground truth" serves as the benchmark against which the PWT segmentation is compared.

The segmentation result of the PWT algorithm indicates that one region was generated to represent the unbroken tibia. The surface of this region looks very similar to the ground truth one. The cut discrepancy metric for the segmentation result is 0.05. This low value confirms the similarity between the segmented region and the ground truth one.

Figures (18-21) show segmentation result for a 3D CT image for a fractured tibia that was broken into three fragments using the PWT algorithm. Figure (18) shows all fragments together while each fragment is viewed sepa-

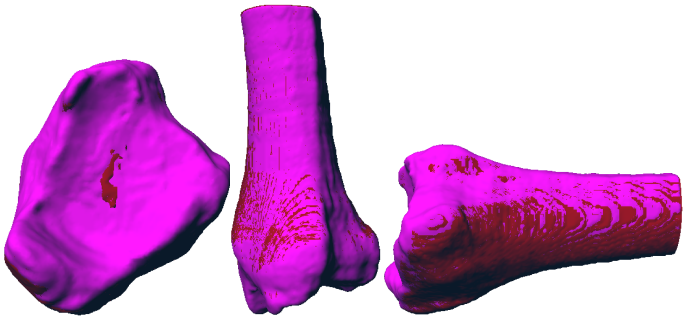

(a) (b) (c)

Figure 17: The segmentation results for a 3D CT image for unbroken tibia using the PWT algorithm and its "ground truth" segmentation. The PWT segmentation result is shown in red, while the "ground truth" segmentation is shown in pink. They are shown together to allow for visual comparison of the results and to better understand the strengths and weaknesses of the PWT algorithm.

| Fragment | First | Second | Third |
|---|---|---|---|
| CC | 0.09 | 0.22 | 0.38 |

Table 4: The cut discrepancy metric values measured for the segmentation result for a 3D CT image for a broken tibia that was fractured into three fragments. The first, second, and third fragments are shown in figures (19-21), respectively.

rately in figures (19-21). The segmentation result is shown from three different view perspective: axial, sagittal, and coronal. The segmentation result and the human generated segmentation, i.e., "ground truth", are shown together to allow for visual comparison of the results. Different segmented regions are shown in different colors.

The segmentation result indicates that five regions were generated to represent the three fracture tibia fragments. Each ground truth fragment is compared with the segmented fragment that has the largest overlap with it. The cut discrepancy metric for each fragment is shown in table (4). The extra two segmented fragments are considered segmentation errors that are explained next.

The proposed algorithm showed two weaknesses during the tests: 1) it

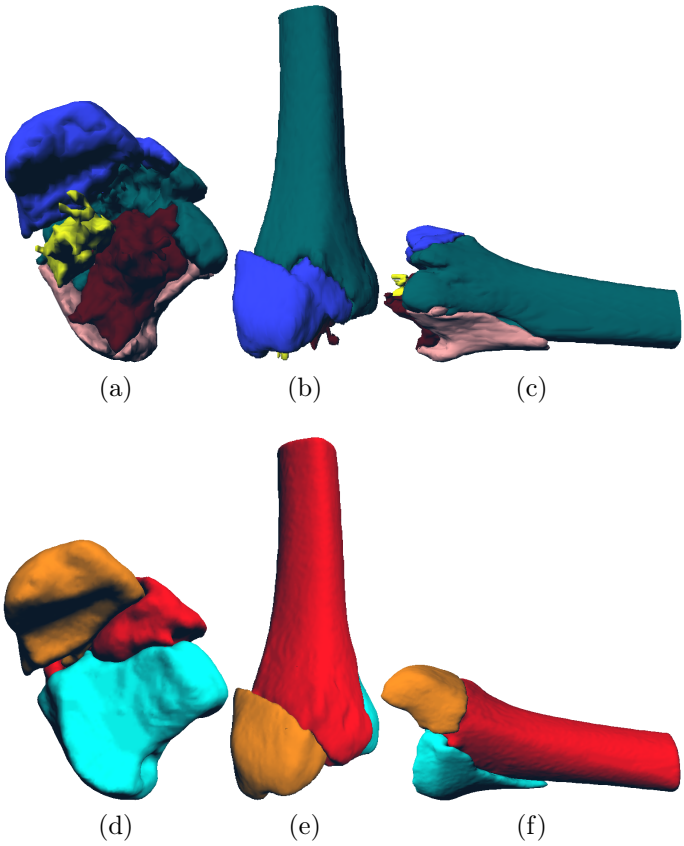


Figure 18: The segmentation results for a 3D CT image for a broken tibia using the PWT algorithm and its "ground truth" segmentation. Figures (a-c) show the segmentation result for all fractured tibia fragments from three different view perspective: axial, sagittal, and coronal, respectively. Figures (d-f) show the human generated segmentation which is treated as "ground truth" from three different view perspective: axial, sagittal, and coronal, respectively. Different segmented regions are shown in different colors.

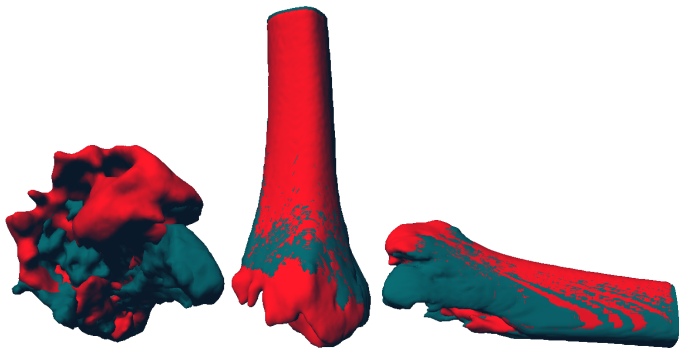

(a) (b) (c)

Figure 19: The segmentation results for the first fragment of three within a 3D CT image for a broken tibia using the PWT algorithm and its corresponding "ground truth" segmentation. Figures (a-c) show the segmentation result from three different view perspective: axial, sagittal, and coronal, respectively. The PWT segmentation result is shown in dark blue, while the "ground truth" segmentation is shown in red.

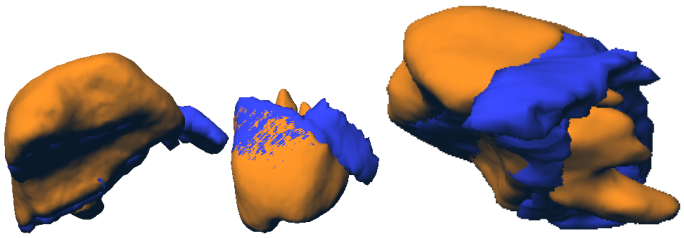

(a) (b) (c)

Figure 20: The segmentation results for the second fragment of three within a 3D CT image for a broken tibia using the PWT algorithm and its corresponding "ground truth" segmentation. Figures (a-c) show the segmentation result from three different view perspective: axial, sagittal, and coronal, respectively. The PWT segmentation result is shown in blue, while the "ground truth" segmentation is shown in orange.

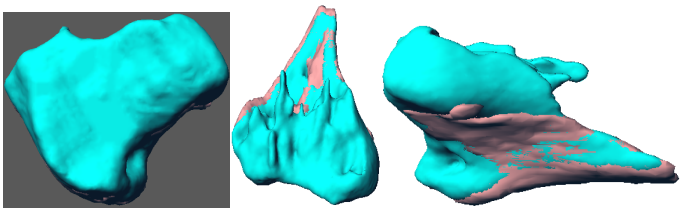

(a) (b) (c)

Figure 21: The segmentation results for the third fragment of three within a 3D CT image for a broken tibia using the PWT algorithm and its corresponding "ground truth" segmentation. Figures (a-c) show the segmentation result from three different view perspective: axial, sagittal, and coronal, respectively. The PWT segmentation result is shown in blue, while the "ground truth" segmentation is shown in salmon color.

may generates an incorrect number of bone fragments, and 2) it may not perform well on segmenting small bone fragments.

For the first weakness, the proposed segmentation algorithm may generate an incorrect number of segments due to an error in detecting the correct number of markers for bone fragment segments in the classification process stage, refer to section (3.1). This can be explained, in part, due to two reasons: 1) the existence of low intensity cortex areas within the cortex region and 2) the minimum intensity value considered a cortical tissue is too low value. These reasons may divide a single cortex region into multiple ones or may connect multiple disjoint regions together by assuming pixels that do not belong to a cortical tissue as cortical pixels. So an incorrect number of markers is generated, hence the incorrect number of segments..

For the second weakness, the proposed segmentation algorithm may not perform well in segmenting small bone fragment for two main reasons: 1) the ratio of the size of the cortex region with respect to the size of the segment is relatively small for small fragments and 2) the width of a bone region for a small fragment is relatively small. For the first reason, having a small cortex region in a fragment segment generates a relatively small marker with respect to the size of that intended segment. So the pixels that belong to that intended segment may have large distances to the marker region causing them to have low fragment likelihood values according to equation (1). Pixels with low likelihood values for a marker are less likely labeled with the label

of that marker especially when they are close to other markers. So, these pixels are highly likely labeled with incorrect labels. For the second reason, having a bone region with small width increases the number of pixels that are likely to be inside "isthmus" bone areas in that region. These pixels are given low probability values according to equation (11). As a result, the pixels that are assumed to be inside "isthmus" bone areas are labeled last in the PWT algorithm and they are divided evenly between the neighboring segments causing some of these pixels to be incorrectly labeled.

Furthermore, the algorithm is not able to estimate bone fragments that contains cancellous bone tissue only, and may be affected by the noise caused beam hardening from a cast. For the first situation, the algorithm either ignores the cancellous-only fragments if they are not attached to any marker or merge their regions with other attaching neighboring fragment regions. For the second situation, the algorithm may generate false markers due to the existence of beam hardening noise. This noise is reduced by ignoring markers located outside the limb or ignoring markers with too high intensity values. Metal objects appear so bright in CT images.

## 5. Conclusions

A novel segmentation algorithm is presented to segment bone fragments within CT images using the PWT. The new bone segmentation algorithm presents a unique likelihood probability that is based on intensity and position information of the image pixels to increase the algorithm robustness to image inhomogeneities. The algorithm also introduces an original solution to leak problem through "isthmus" bone areas by detecting pixels in these areas of the bone region in the image and processing them last in the algorithm. The algorithm parameters are the values for minimum intensities for cortical and cancellous regions in the CT image which are set during the calibration process of the imaging device. These parameters are easy to understand and control which make the algorithm intuitive for clinical applications. The conducted experiments to extract bone fragments from CT images show the benefits of the presented algorithm to leading segmentation algorithms. Also, the algorithm is applied in a medical application to extract tibia and fibula bone fragments from CT image stacks. The presented algorithm showed a convincing accuracy which suggests that the algorithm could be used in different medical image segmentation problems.

## References


Arabi, H., Zaidi, H., 2017. Comparison of atlas-based techniques for whole-body bone segmentation. Medical Image Analysis 36, 98 – 112. doi:http://dx.doi.org/10.1016/j.media.2016.11.003.

Aslan, M.S., Ali, A., Arnold, B., Fahmi, R., Farag, A.A., Xiang, P., 2009. Segmentation of trabecular bones from vertebral bodies in volumetric CT spine images, in: 2009 16th IEEE International Conference on Image Processing (ICIP), pp. 3385–3388. doi:10.1109/ICIP.2009.5413887.

Barrett, H., Swindell, W., 1996. Radiological Imaging: The Theory of Image Formation, Detection, and Processing. v. 1, Elsevier Science.

Brahim, W., Mestiri, M., Betrouni, N., Hamrouni, K., 2017. Malignant pleural mesothelioma segmentation for photodynamic therapy planning. Computerized Medical Imaging and Graphics doi:http://dx.doi.org/10.1016/j.compmedimag.2017.05.006.

Burghardt, A.J., Kazakia, G.J., Majumdar, S., 2007. A local adaptive threshold strategy for high resolution peripheral quantitative computed tomography of trabecular bone. Annals of Biomedical Engineering 35, 1678–1686.

Chen, C., Jin, D., Zhang, X., Levy, S.M., Saha, P.K., 2017. Segmentation of Trabecular Bone for In Vivo CT Imaging Using a Novel Approach of Computing Spatial Variation in Bone and Marrow Intensities. Springer International Publishing, Cham. pp. 3–15.

Chen, X., Golovinskiy, A., Funkhouser, T., 2009. A benchmark for 3D mesh segmentation. ACM Transactions on Graphics (Proc. SIGGRAPH) 28.

Chu, C., Bai, J., Wu, X., Zheng, G., 2015. Mascg: Multi-atlas segmentation constrained graph method for accurate segmentation of hip CT images. Medical Image Analysis 26, 173 – 184. doi:http://dx.doi.org/10.1016/j.media.2015.08.011.

Feeman, T., 2009. The Mathematics of Medical Imaging: A Beginners Guide. Springer Undergraduate Texts in Mathematics and Technology, Springer.

Fornaro, J., Keel, M., Harders, M., Marincek, B., Szekely, G., Frauenfelder, T., 2010. An interactive surgical planning tool for acetabular fractures: initial results. Journal of Orthopedic Surgery and Research 5.

Grau, V., Mewes, A., Alcaniz, M., Kikinis, R., Warfield, S., 2004. Improved watershed transform for medical image segmentation using prior information. Medical Imaging, IEEE Transactions on 23, 447 –458.

Hansen, C., Johnson, C., 2005. The Visualization Handbook. Referex Engineering, Butterworth-Heinemann.

Janc, K., Tarasiuk, J., Bonnet, A.S., Lipinski, P., 2011. Semi-automated algorithm for cortical and trabecular bone separation from CT scans. Computer Methods in Biomechanics and Biomedical Engineering 14, 217–218. doi:10.1080/10255842.2011.595192.

Li, C., Jin, D., Chen, C., Letuchy, E.M., Janz, K.F., Burns, T.L., Torner, J.C., Levy, S.M., Saha, P.K., 2015. Automated cortical bone segmentation for multirow-detector ct imaging with validation and application to human studies. Medical Physics 42, 4553–4565. doi:10.1118/1.4923753.

Liu, P., 2012a. A System For Computational Analysis And Reconstruction Of 3D Comminuted Bone Fractures. Ph.D. thesis. The University of North Carolina At Charlotte.

Liu, P., 2012b. A System For Computational Analysis And Reconstruction Of 3D Comminuted Bone Fractures. Ph.D. thesis. The University of North Carolina At Charlotte.

Meyer, F., 1991. Un algorithme optimal de ligne de partage des eaux, in: Reconnaissance des Formes et Intelligence Artificielle, 8e congr‘es, AFCET. pp. 847–857.

Mookiah, M.R.K., Acharya, U.R., Chua, C.K., Min, L.C., Ng, E., Mushrif, M.M., Laude, A., 2013. Automated detection of optic disk in retinal fundus images using intuitionistic fuzzy histon segmentation. Proceedings of the Institution of Mechanical Engineers, Part H: Journal of Engineering in Medicine 227, 37–49.

Otsu, N., 1979. A threshold selection method from gray-level histograms. IEEE Transactions on Systems, Man and Cybernetics 9, 62–66.

Paulano, F., Jiménez, J., Pulido, R., 2014. 3D segmentation and labeling of fractured bone from CT images. The Visual Computer , 1–10.

Perez-Carrasco, J.A., Acha-Pinero, B., Serrano, C., 2015. Segmentation of bone structures in 3D CT images based on continuous max-flow optimization. doi:10.1117/12.2082139.

Porikli, F., Kocak, T., 2007. Fast distance transform computation using dual scan line propagation, in: SPIE Conference Series.

Powers, D.M.W., 2007. Evaluation: From Precision, Recall and F-Factor to ROC, Informedness, Markedness & Correlation. Technical Report SIE-07-001. School of Informatics and Engineering, Flinders University. Adelaide, Australia.

Schmid, J., Kim, J., Magnenat-Thalmann, N., 2011. Robust statistical shape models for MRI bone segmentation in presence of small field of view. Medical Image Analysis 15, 155 – 168. doi:http://dx.doi.org/10.1016/j.media.2010.09.001.

Shadid, W., Willis, A., 2013. Bone fragment segmentation from 3D CT imagery using the probabilistic watershed transform, in: Southeastcon, 2013 Proceedings of IEEE, pp. 1–8.

Swierczynski, P., Papiez, B.W., Schnabel, J.A., Macdonald, C., 2017. A level-set approach to joint image segmentation and registration with application to CT lung imaging. Computerized Medical Imaging and Graphics doi:http://dx.doi.org/10.1016/j.compmedimag.2017.06.003.

Valentinitsch, A., Patsch, J.M., Deutschmann, J., Schueller-Weidekamm, C., Resch, H., Kainberger, F., Langs, G., 2012. Automated threshold-independent cortex segmentation by 3d-texture analysis of hr-pqct scans. Bone 51, 480 – 487.

Wu, J., Belle, A., Hargraves, R.H., Cockrell, C., Tang, Y., Najarian, K., 2014. Bone segmentation and 3D visualization of CT images for traumatic pelvic injuries. International Journal of Imaging Systems and Technology 24, 29–38.